

Evolution of eccentricity and inclination of hot protoplanets embedded in radiative discs

Henrik Eklund,¹* Frédéric S. Masset²

¹*Department of Physics, Gothenburg University, Origovägen 6 b, 41296 Gothenburg, Sweden*

^{1,2}*Instituto de Ciencias Físicas, Universidad Nacional Autónoma de México, Av. Universidad s/n, 62210 Cuernavaca, Mor., Mexico*

Accepted 2017 April 4. Received 2017 April 2; in original form 2017 January 30

ABSTRACT

We study the evolution of the eccentricity and inclination of protoplanetary embryos and low-mass protoplanets (from a fraction of an Earth mass to a few Earth masses) embedded in a protoplanetary disc, by means of three dimensional hydrodynamics calculations with radiative transfer in the diffusion limit. When the protoplanets radiate in the surrounding disc the energy released by the accretion of solids, their eccentricity and inclination experience a growth toward values which depend on the luminosity to mass ratio of the planet, which are comparable to the disc’s aspect ratio and which are reached over timescales of a few thousand years. This growth is triggered by the appearance of a hot, under-dense region in the vicinity of the planet. The growth rate of the eccentricity is typically three times larger than that of the inclination. In long term calculations, we find that the excitation of eccentricity and the excitation of inclination are not independent. In the particular case in which a planet has initially a very small eccentricity and inclination, the eccentricity largely overruns the inclination. When the eccentricity reaches its asymptotic value, the growth of inclination is quenched, yielding an eccentric orbit with a very low inclination.

As a side result, we find that the eccentricity and inclination of non-luminous planets are damped more vigorously in radiative discs than in isothermal discs.

Key words: planet-disc interactions – protoplanetary discs – hydrodynamics – radiative transfer – planets and satellites: dynamical evolution and stability

1 INTRODUCTION

When a low-mass protoplanet perturbs its parent protoplanetary disc solely by gravity, its eccentricity and inclination are usually damped. The damping time scale of these quantities is, for an Earth mass planet embedded in a disc similar to the Minimum Mass Solar Nebula, of order of a thousand years at a few astronomical units. This small time scale is shorter, by a factor of h^{-2} (h being the disc’s aspect ratio) than the migration time scale (Artymowicz 1993). In the limit of vanishing eccentricity and inclination, the damping rates can be estimated by an expansion of the perturbing potential to first order in e and i . This was the approach of Tanaka & Ward (2004) who evaluated these rates for a planet in an isothermal disc by means of semi-analytical, linear calculations. When these orbital elements are not negligible compared to the disc’s aspect ratio, it is necessary to include higher order terms. This was done by Papaloizou & Larwood (2000), who included all resonances necessary for

convergence, and who considered for the first time eccentricities larger than the disc’s aspect ratio. For very high eccentricities, however, a resonant approach becomes unpractical and one may rather resort to a dynamical friction calculation (Papaloizou 2002a; Muto et al. 2011), as the disc response is local, and the Keplerian shear unimportant. Numerical simulations have been employed to confirm and extend analytical predictions (Cresswell et al. 2007), and have allowed to relax the customary isothermal approximation (Bitsch & Kley 2010, 2011). In all cases the disc’s tide has been found to damp eccentricity and inclination.

Not all the disturbances imparted to the disc by a protoplanetary embryo are due to gravity. Benítez-Llambay et al. (2015) have recently investigated the impact on planetary migration of heat release by a hot, accreting embryo in the surrounding disc, and found that this effect is able to revert the migration of embryos up to a few Earth masses. This study was however limited to planets on circular orbits. By a dynamical friction calculation, Masset & Velasco Romero (2017) have studied a perturber that travels across a uniform, gaseous and opaque medium, and that releases heat

* E-mail: eklhen@gmail.com

at a fixed rate in the surrounding gas. They found that the hot, underdense trail thus triggered in the gas exerts a force on the perturber (dubbed the heating force) directed along its motion, and independent of the perturber’s velocity in the limit of low Mach numbers. Applying this result to embedded protoplanetary embryos, they suggest these could reach eccentricities and inclinations comparable to the disc’s aspect ratio. Whether a dynamical friction calculation in a disc is justified, however, depends on the competition between two time scales: the response time scale and the shear time scale. When the latter is larger than the former, the shear is unimportant and one can resort to a calculation of dynamical friction. In the case of the hot plume, this should occur for values of the eccentricity largely smaller than the disc’s aspect ratio (Masset & Velasco Romero 2017). We will confirm this expectation in the present work. The disc’s tide¹, however, can only be captured by a dynamical friction calculation for eccentricities in excess of the disc’s aspect ratio (Papaloizou 2002b; Muto et al. 2011). The asymptotic values of eccentricity and inclination quoted by Masset & Velasco Romero (2017), obtained through a dynamical friction calculation both for the hot trail and for the tide of the ambient gas, may therefore not be accurate, as they are comparable to the disc’s aspect ratio. The purpose of the present work is to investigate, by means of numerical simulations, whether hot, embedded embryos are indeed subjected to an eccentricity and inclination growth, and which values these orbital elements can reach at larger time.

Our paper is organised as follows. In Section 2 we describe our setup and the numerical methods employed. In Section 3 we investigate the eccentricity and inclination behaviour of non-luminous embryos, firstly in isothermal discs so as to validate our numerical procedures by comparing our code’s outcome to the analytical expressions of Tanaka & Ward (2004), and secondly in a radiative disc similar to the one that will be considered throughout the rest of the paper. In Section 4 we present our results for luminous embryos. These consist of fiducial calculations (one for the eccentricity, one for the inclination), and of different explorations of parameter space. Namely we explore the impact of the initial value of eccentricity or inclination, the planetary mass, and the mass accretion rate. We also present long term calculations, spanning 2000 or 2500 orbital periods, in which we consider planets that are simultaneously eccentric and inclined. We discuss our results in Section 5 and draw our conclusions in Section 6.

2 SETUP

In this section we present the different parts of our setup and the numerical methods employed.

2.1 Disc

We consider a protoplanetary disc around a central star of mass M_\star . We denote its aspect ratio with $h = H/r$, where

¹ Throughout this paper, we call disc’s tide the force exerted on the planet by the perturbation that would be induced in the disc if the planet was non-luminous.

H is the pressure scale length of the disc and r is the radial distance from the star. The surface density of the disc is given by:

$$\Sigma(r) = \Sigma_0 \left(\frac{r}{r_0} \right)^{-p}, \quad (1)$$

where Σ_0 is the surface density at $r = r_0$ and where we adopt a slope of surface density $p = 1$. The disc has a constant opacity $\kappa = 1.0 \text{ cm}^2 \text{ g}^{-1}$ and a constant kinematic viscosity $\nu = 1.016 \times 10^{15} \text{ cm}^2 \text{ s}^{-1}$, which translates into an α -value (Shakura & Sunyaev 1973) of $4 \cdot 10^{-3}$ for our isothermal discs, and $5.6 \cdot 10^{-3}$ for our radiative discs, which have a slightly different thickness. In this first, exploratory work, the opacity is kept to this fixed value in order not to introduce an additional, complex dependence of the disc’s thermal diffusivity on its temperature and density.

2.2 Planet

A planet with mass M_p is inserted in the disc on an orbit around the central star with a semi-major axis $a = 5.2 \text{ au}$ (astronomical units). We denote by e and i its eccentricity and inclination, respectively, and by e_0 and i_0 the initial values of these orbital elements. All values quoted for the inclination throughout this paper are in radians. The planet is freely moving in the disc. It is heated up by the bombardment of infalling objects, such as planetesimals or pebbles. We assume the latent heat for vaporisation of the infalling bodies to be a small fraction of their potential energy, which is a reasonable assumption for planets in the Earth mass range (Benítez-Llambay et al. 2015). We also assume that if infalling bodies are destroyed far above the planetary surface, their debris eventually reach the surface, thereby ultimately releasing the potential energy GM_p/R_p per unit mass, where R_p is the physical radius of the planet. This assumption is known as the sinking hypothesis (Pollack et al. 1996). The luminosity of the planet thus reads:

$$L = \frac{GM_p \dot{M}_p}{R_p}, \quad (2)$$

where G is the gravitational constant and \dot{M}_p the planetary accretion rate. We introduce the mass doubling time:

$$\tau = \frac{M_p}{\dot{M}_p}, \quad (3)$$

so that the luminosity is given by:

$$L = \frac{GM_p^2}{R_p \tau}. \quad (4)$$

The planet’s physical radius is evaluated assuming a homogeneous mass distribution with density $\rho_p = 3 \text{ g cm}^{-3}$. Our results do not depend sensitively on this assumption, since the planet’s physical radius scales with the cubic root of the mean density.

2.3 Numerical setup

We use the public code FARGO3D² (Benítez-Llambay & Masset 2016) with orbital advection enabled (Masset 2000).

² <http://fargo.in2p3.fr>

The version of the code that we used includes a non-public radiative transfer module. We use a spherical mesh with azimuthal extent $[-\phi_{\max}, \phi_{\max}]$, where ϕ_{\max} depends on the run and will be specified later. The radial extent is $[3/5a, 7/5a]$ and the extent in colatitude is $[\pi/2 - 0.12, \pi/2 + 0.12]$. We use $N_r = 512$ cells in radius, $N_\theta = 128$ cells in colatitude, and a number of cells in azimuth N_ϕ that depends on ϕ_{\max} : when $\phi_{\max} = \pi$ (i.e. when we simulate a full disc), we use $N_\phi = 1024$ cells. Our resolution respectively in azimuth, radius and colatitude is therefore: $(\Delta\phi, \Delta r, \Delta\theta) = (6.1 \cdot 10^{-3}, 1.6 \cdot 10^{-3}a, 1.9 \cdot 10^{-3})$. We soften the planetary potential over a length $\epsilon = 1.5 \cdot 10^{-3}a$, comparable to our radial resolution. When ϕ_{\max} differs from π , we adjust the number of cells in azimuth so as to keep $\Delta\phi$ constant. When simulating radiative discs, radiative transfer is dealt with in the same manner as in [Benítez-Llambay et al. \(2015\)](#). We use wavelength-independent flux limited diffusion with a two-temperature approach ([Bitsch et al. 2013](#)). The frame in which our calculations are performed corotates with the planet, hence it has a time-varying rotation rate whenever the planet is either eccentric or inclined.

At each timestep Δt , the energy released by the planet $\Delta E = L\Delta t$ is used to increase the internal energy in the cells surrounding the planet, in a separate substep. The distribution of ΔE among each of the eight neighbouring cells is determined using a virtual cell centred on the planet, with same size as the neighbouring cells. The fraction of this cell's volume occupied by each of the neighbours determines the fraction of ΔE that is attributed to this neighbour. This procedure implies that the barycentre of the energy released lies at the planet location. In the calculation of the different fractions, we neglect the mesh curvature since the energy release is a very local process that takes place on eight neighbouring cells at most. Our heat release occurs on the smallest possible scale allowed by the mesh. The force exerted by the heated region will be accurately captured if the size of this region is much larger than the resolution of the mesh. We will study this requirement in more detail in section 4.5.

3 PRELIMINARY STUDY

In a first step, we check the behaviour of the planet without heat release. We do this firstly in a locally isothermal disc, so as to compare our results with the analytic estimates of [Tanaka & Ward \(2004\)](#), then in a radiative disc. In each case six runs are performed in which the orbit of the planet is initially set either with eccentricities $e = 0.01, 0.015$ and 0.02 or with inclinations $i = 0.01, 0.015$ and 0.02 radians. The planet is free to move in all direction. However we spawn eccentric planets coplanar with the disc, and inclined planets on circular orbits, so as to study the time evolution of the orbital elements in a separate manner. Our simulations are evolved for 5 orbits of the planet only. This amount of time appears to be sufficient to allow a precise measurement of the variation rate of the orbital elements under study.

3.1 Isothermal disc

In this study we use a disc with a uniform aspect ratio $h = 0.05$, while our planet has a mass $3 \cdot 10^{-6}M_\star$, which translates into one Earth mass if the central star has a solar mass. We

cast our results in terms of the characteristic time ([Tanaka & Ward 2004](#)):

$$t_c = q^{-1} \left(\frac{\Sigma_0 a^2}{M_\star} \right)^{-1} \left(\frac{c_s}{a\Omega_p} \right)^4 \Omega_p^{-1}, \quad (5)$$

where $q = M_p/M_\star$ and c_s is the sound speed at the radius of the planet and Ω_p the planet's orbital frequency. Our results are shown in Fig. 1. We also determine the precession rates of the periapsis and of the line of nodes, respectively for eccentric and inclined cases. Our largest difference with the results of [Tanaka & Ward \(2004\)](#) is found on the eccentricity damping rate, and amounts to 17 %. The vertical extent of our mesh, which is $\pm 2.4h$, only contains 98 % of the column density of the full disc, so we do not expect a match better than to a few percents. Globally, these results are in very satisfactory agreement with the analytic expressions of [Tanaka & Ward \(2004\)](#).

3.2 Radiative disc

The study of heat release that will be presented in section 4 is performed in a radiative disc. Here we study the inclination and eccentricity evolution of a planet without heat release in a radiative disc. Prior to the simulations with a planet, the radiative disc is relaxed toward hydrostatic and radiative equilibria by means of two-dimensional runs in the (r, θ) plane. From now on we specialise to the case of a central object of solar mass ($M_\star = M_\odot$), and to the values $a = r_0 = 5.2$ au, $\Sigma_0 = 200$ g cm $^{-2}$. The ratio of specific heats at constant pressure and constant volume is $\gamma = 1.4$. After convergence toward equilibrium, we obtain an aspect ratio at the planet location of $h_r = 0.042$, close to the value given by [Bitsch et al. \(2013\)](#):

$$h = \left(\frac{9}{32} \frac{\mathcal{R}^4}{\mu^4} \kappa \nu \Sigma_0^2 \frac{r_0}{G^3 M_\star^3 \sigma} \right)^{1/8} = 0.043 \quad (6)$$

where \mathcal{R} the ideal gas constant, σ the Stefan constant and $\mu = 2.3$ g mol $^{-1}$ is the mean molecular weight. As the disc mostly settles vertically its surface density profile is essentially unchanged with respect to the initial conditions, given by Eq. (1). Once the disc has reached equilibrium, a planet of one Earth mass ($M_p = M_\oplus$) is inserted at $r_0 = 5.2$ au and let free to evolve through the disc. Our setup is essentially similar to that of [Benítez-Llambay et al. \(2015\)](#), except that we relax the assumption of circular and coplanar orbits. As previously, the variation of its orbital elements is subsequently measured over five orbits. The rates of change measured for e and i differ much from the isothermal case, as can be seen in column 3 of Table 1. We normalise the damping rates with:

$$t_c = q^{-1} \left(\frac{\Sigma_0 a^2}{M_\star} \right)^{-1} h_r^4 \Omega_p^{-1} = 3.2 \text{ kyrs} \quad (7)$$

The damping rates, both for the eccentricity and inclination, are significantly in excess of those found in isothermal discs (see section 3.1), and they display a trend to be larger when the corresponding orbital element is smaller. This is in sharp contrast with the results of [Bitsch & Kley \(2010\)](#), although these are not directly comparable to ours, since these authors considered a large mass planet with $q/h^3 \sim 1.2$, whereas we are concerned here with low mass, embedded objects. This

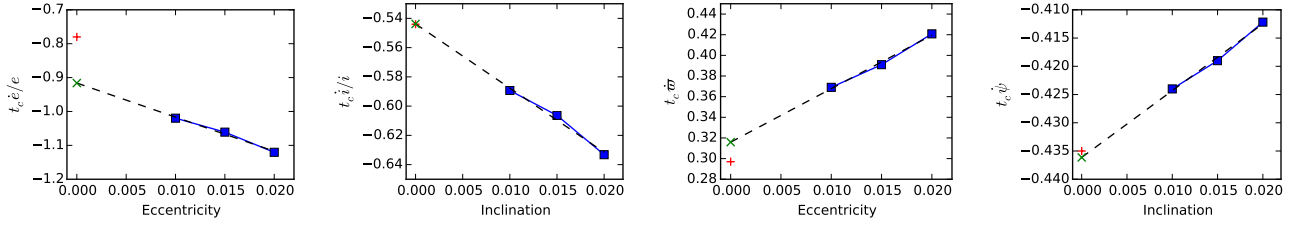


Figure 1. From left to right: eccentricity damping rate, inclination damping rate, rate of precession of periapsis for an eccentric planet, and rate of precession of the line of nodes for an inclined planet, in an isothermal disc. In each plot these quantities are displayed as a function either of eccentricity or inclination. Also shown with a \times sign is the value for a vanishing eccentricity or inclination, extrapolated from the simulations data with a linear regression fit (dashed lines). We show with a $+$ sign the value given by [Tanaka & Ward \(2004\)](#).

behaviour is the subject of current investigation, the results of which will be presented in a forthcoming publication. We note that $h_r = c_s^{\text{iso}}/(r\Omega_p)$, where c_s^{iso} is the isothermal sound speed, so that Eq. (7) is equivalent to Eq. (5) when $c_s \equiv c_s^{\text{iso}}$. If we had used the adiabatic sound speed in Eq. (7), the time scale t_c would be larger by a factor $\gamma^2 \sim 2$. This would compound the difference with the isothermal results. We stress that our choice of the expression of t_c is only a choice of normalisation which does neither affect our conclusions nor the outcomes of the runs.

3.2.1 Reduction of the azimuthal extent

Since our study involves a significant exploration of parameter space, the reduction of the cost per simulation is a concern. We investigate how the results for a full disc in azimuth ($\phi_{\text{max}} = \pi$) are affected when one considers only a quadrant in azimuth ($\phi_{\text{max}} = \pi/4$), keeping the same resolution (using therefore only 256 cells in this direction instead of 1024). When doing so it is important that the frame corotates with the planet (so that the planet lies on the bisector of the quadrant at any instant in time), and that the azimuthal averaged density be subtracted from each cell prior to the evaluation of the disc's force onto the planet ([Baruteau & Masset 2008](#)).

Calculations restricted to a quadrant give the evolution rates of Table 1 in column 4. The eccentricity damping rates display changes with respect to the full disc calculations at the percent level, while the inclination damping rates are reduced by approximately 10 %. We consider these variations acceptable, and perform the rest of our simulations on a quadrant.

We comment that the impact of the circular resonances³ on the eccentricity evolution is marginal. The driving or damping timescales of these resonances are comparable to the migration timescale, hence a factor h^{-2} larger than the timescale associated to the eccentric Lindblad and corotation resonances, which are first order in the eccentricity, and which play the most important role for a non-luminous planet. We therefore anticipate that an accurate description of the torque arising from the circular resonances should

³ The resonances that exist even when the planet is on a circular orbit, such as the coorbital corotation resonances or the Lindblad resonances associated with the angular frequency of the planet's guiding centre. These are the resonances that drive the migration of a planet on a nearly circular orbit.

Table 1. Eccentricity and inclination damping rates in radiative discs simulated over a full mesh (F) and over a quadrant only (Q). The second column shows the analytic estimates of [Tanaka & Ward \(2004\)](#) for low values of the eccentricity and inclination. The rates measured in the simulations are given for three different initial values of the corresponding orbital element. Column 3 gives the evolution rates for the full disc, column 4 for the quadrant and column 5 shows the ratio of columns 3 and 4.

e_0	$t_c \frac{\dot{e}}{e} \Big _{TW04}$	$t_c \frac{\dot{e}}{e} \Big _F$	$t_c \frac{\dot{e}}{e} \Big _Q$	$\frac{(\dot{e}/e)_F}{(\dot{e}/e)_Q}$
$\rightarrow 0$	-0.78			
0.010		-1.75	-1.73	1.01
0.015		-1.45	-1.44	1.01
0.020		-1.27	-1.26	1.01
i_0	$t_c \frac{\dot{i}}{i} \Big _{TW04}$	$t_c \frac{\dot{i}}{i} \Big _F$	$t_c \frac{\dot{i}}{i} \Big _Q$	$\frac{(\dot{i}/i)_F}{(\dot{i}/i)_Q}$
$\rightarrow 0$	-0.54			
0.010		-0.97	-0.89	1.09
0.015		-0.85	-0.77	1.10
0.020		-0.77	-0.69	1.11

be unimportant for the process we describe in this work, which occurs on time scales shorter than that of migration. This comment applies in particular to the coorbital corotation torque or its non-linear version, the horseshoe drag ([Paardekooper & Papaloizou 2009](#)). Nonetheless, it should be kept in mind that studies of the migration of hot planets with our setup (which is not the primary scope of this work) may be biased by two effects:

- Working on a restricted domain in azimuth shortens the horseshoe libration time, and consequently affects the ratio of this time to the viscous time across the horseshoe region, which controls the degree of saturation of the horseshoe drag ([Masset 2001](#); [Masset & Casoli 2010](#); [Paardekooper et al. 2011](#)).

- The horseshoe region is not resolved for planets with masses lower than $O(10^{-1}) M_{\oplus}$, resulting in an incorrect tidal torque from the disc. For such low masses, however, migration is very slow and hardly relevant at all.

4 STUDY OF HEAT RELEASE

We present in this section the evolution rates of eccentricity and inclination of a planet that is releasing heat into the sur-

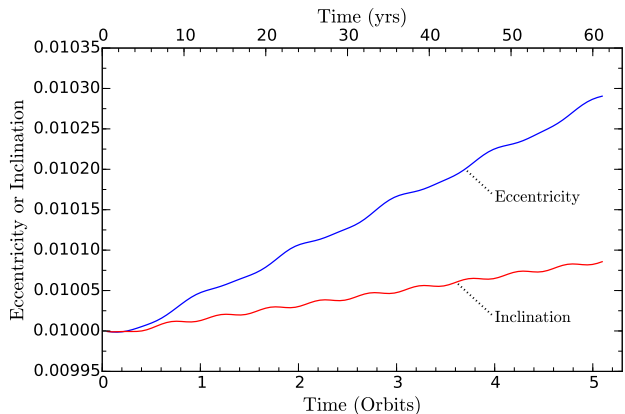


Figure 2. Evolution of the eccentricity and the inclination of the luminous planet of the fiducial calculations.

rounding disc. In section 4.1 we firstly present our fiducial calculations. Subsequently, we explore the behaviour of the evolution rates as a function of several parameters. These parameters are the initial values of the eccentricity and the inclination (section 4.2), the planetary accretion rate (section 4.3) and the planetary mass (section 4.4). All the evolution rates presented here are mean values over the first five orbits after the planet is inserted into the disc. In section 4.5 we examine the temperature excess due the heat release for an eccentric and an inclined planet. Finally, in section 4.6 we explore the long-term behaviour of the eccentricity and inclination of a hot planet.

4.1 Fiducial calculations

Our two fiducial calculations (one for the eccentricity, another one for the inclination) have same parameters as the ones used in section 3.2. In addition, we set for the planet a mass doubling time of 10^5 yrs, which determines its luminosity through Eq. (4). This mass doubling time lies within the admitted range of mass doubling times for Earth-sized protoplanets at a distance of 5.2 au, and represents a conservative value typical of planetesimal accretion (Pollack et al. 1996) rather than the more efficient pebble accretion (Lambrechts & Johansen 2012). The full set of parameters is summed up in Table 2 for the reader’s convenience.

The time evolution of the eccentricity and inclination is shown in Figure 2. Both quantities steadily increase. The rate of change of the eccentricity is $t_c \dot{e}/e = +1.57$, that of the inclination is $t_c \dot{i}/i = +0.48$ and thus the eccentricity broadly increases three times faster than the inclination.

4.2 Varying the initial value of eccentricity or inclination

We study hereafter the dependence of the driving rate of either the eccentricity or inclination upon its initial value. An immediate application of such study is that it allows to mimic, in a piecewise fashion, a long-term evolution by connecting one after another short term graphs extrapolated to the next available initial eccentricity or inclination, so as

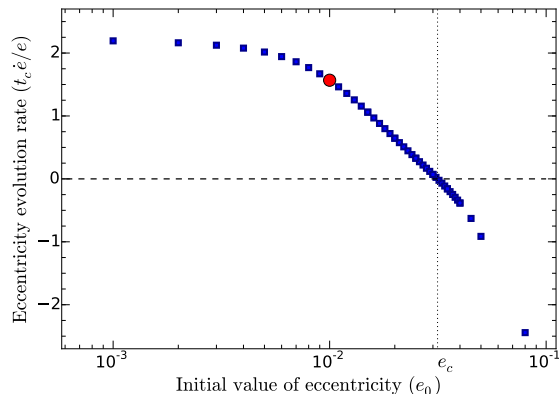


Figure 3. Time derivative of eccentricity as a function of eccentricity. The fiducial calculation is shown with a red disc. The eccentricity is found to have a null time derivative for the critical value $e_c \approx 0.0315$.

to infer the behaviour of the orbital element at larger time (this implicitly assumes that the driving rate of the orbital element depends only on its instantaneous value, rather than on its history).

We vary the eccentricity and inclination with respect to their fiducial values as follows. They are set to values ranging between 0.001 and 0.04 by steps of 0.001 and to 0.045, 0.05 and 0.08. The results are presented in Figs. 3 and 4.

We recover the fact that the eccentricity time derivative is broadly three times larger than that of the inclination. Both graphs show an horizontal asymptote at low values ($\lesssim 0.01$), which suggests that both the eccentricity and inclination undergo an exponential growth up to ~ 0.01 . The eccentricity time derivative shows a monotonous behaviour, and a sign reversal at $e = e_c$. This suggests that the eccentricity, if initially smaller than e_c , will grow and tend toward e_c at larger time. Reciprocally, if it is initially larger than e_c , it should decay toward e_c at larger time. Since $t_c \dot{e}/e = O(1)$, one can infer that the characteristic timescale for the variation of e is t_c , which amounts here to a few thousand years, as evaluated in Eq. (7). Similar considerations apply to the inclination, which tends toward a value marginally smaller than e_c .

We note in Fig. 4 that the decay rate of the most inclined case is smaller than could be extrapolated from the data at lower inclination. This is presumably due to the fact that for this case, the planet is out of the disc for a significant fraction of its orbit. This behaviour, in contrast, is not expected, and not found, for the eccentricity (Fig. 3).

4.3 Dependence on the accretion rate

The mass doubling time τ is varied between 1 kyrs and 300 kyrs. The orbital parameters change over a timescale much shorter than the mass doubling time. Thus we do not add the accreted mass to the planetary mass. For each case the mean evolution rates of the eccentricity and inclination are calculated. The eccentricity evolution rates are presented in Figure 5 and the inclination evolution rates in Figure 6. With this specific planet-disc setup of the fiducial run, the

Table 2. Parameters of the fiducial calculations. The planet is inserted in the disc and released at apocentre or on its ascending line of nodes once the disc has reached hydrostatic and thermal equilibrium, at which point the disc has an aspect ratio $h_r = 0.042$ at the location of the planet.

Parameter	Value	Parameter	Value	Parameter	Value
μ	2.3 g mol^{-1}	p	1	N_ϕ	256 cells
ρ_p	3 g cm^{-3}	τ	10^5 yrs	ϕ interval	$[-\pi/4, \pi/4]$
Σ_0	200 g cm^{-2}	M_\star	$1 M_\odot$	N_r	512 cells
(e_0, i_0)	(0.01, 0) or (0, 0.01)	r_0, a	5.2 au	r interval (au)	[3.12, 7.28]
κ	$1 \text{ cm}^2 \text{ g}^{-1}$	M_p	$1 M_\oplus$	N_θ	128 cells
ν	$1.016 \cdot 10^{15} \text{ cm}^2 \text{ s}^{-1}$	γ	1.4	θ interval	$[\pi/2 - 0.12, \pi/2 + 0.12]$

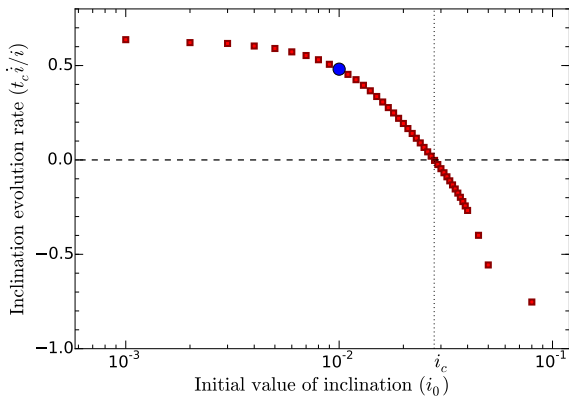


Figure 4. Time derivative of inclination as a function of inclination. The fiducial calculation is shown with a blue disc. The inclination is found to be constant in time at the critical value $i_c \approx 0.028$.

eccentricity increases for mass doubling times shorter than about 240 kyrs. The inclination needs a slightly larger luminosity and increases for mass doubling times shorter than about 200 kyrs. With longer mass doubling times than these, i.e. slower mass accretion or lower luminosities, the luminosity is not large enough to yield an eccentricity or inclination growth, and these orbital parameters would decay below their fiducial initial value of 0.01. However with larger mass doubling times the damping rates are still smaller than those of a cold planet. We explore some very large mass accretion rates that are not realistic, but might account for very large luminosities reached after merger events. We find peak values of the mass accretion at low mass doubling times where the eccentricity and inclination are boosted most rapidly. The corresponding mass doubling times are here 4 kyrs for the eccentricity and 6 kyrs for the inclination.

4.4 Dependence on planetary mass

We vary the planetary mass from $5 \times 10^{-4} M_\oplus$ (about 4 percent of the mass of the Moon) to $7.6 M_\oplus$, while keeping the mass doubling time constant. We note, using Eq. (4), that the luminosity to mass ratio of the planet scales with $M_p^{2/3}$ when τ is kept constant. Our procedure therefore favours large objects, which have a large luminosity to mass ratio. Yet we consider that the mass doubling time is a variable

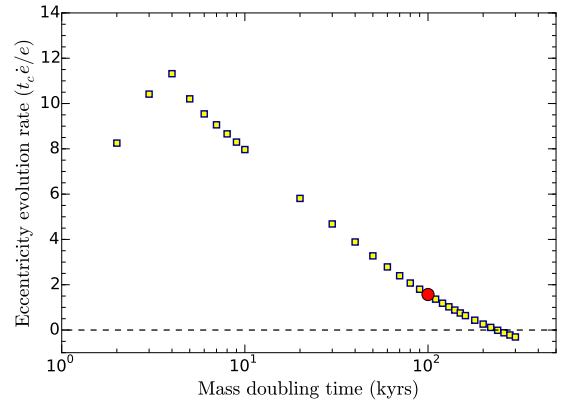


Figure 5. Growth or damping rate of eccentricity as a function of the mass doubling time. The fiducial calculation is indicated with a red disc. For all calculations $e_0 = 0.01$.

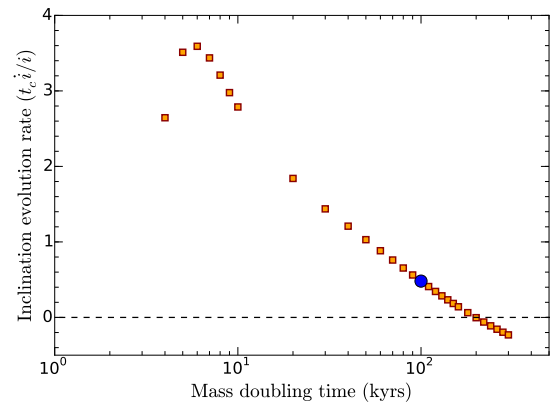


Figure 6. Growth or damping rate of inclination as a function of the mass doubling time. The fiducial calculation is indicated with a blue disc. For all calculations $i_0 = 0.01$.

probably more intuitive than the planet's luminosity, and prefer to explore the planetary mass dependence at fixed τ . The time derivative of the eccentricity is shown in Figure 7 and that of the inclination in Figure 8. With the fiducial mass doubling time $\tau = 10^5 \text{ yrs}$, the eccentricity experiences a growth for planetary masses larger than $M_1 = 0.25 M_\oplus$ and the inclination for planetary masses larger than $M'_1 = 0.31$

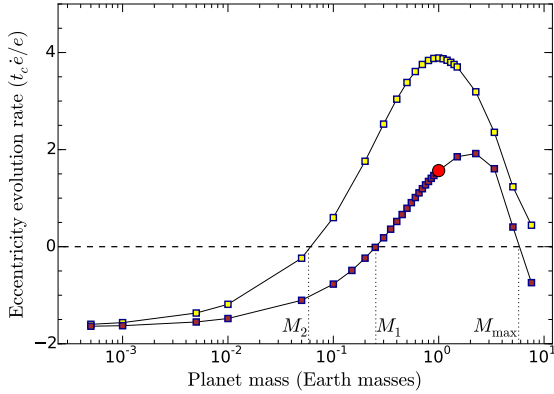


Figure 7. The evolution rate of eccentricity as a function of the planet mass, for two different values of the mass doubling time. The purple markers correspond to $\tau = 10^5$ yrs (the red disc on this series corresponds to the fiducial calculation) and the yellow markers correspond to $\tau = 4 \times 10^4$ yrs.

M_\oplus . We also show the behaviour of the eccentricity for a mass doubling time of $\tau = 4 \times 10^4$ yrs. For all planetary masses considered, the time derivative of the eccentricity is larger than for the fiducial value of τ . We find that, in this case, the eccentricity experiences a growth for planetary masses larger than $M_2 = 0.058 M_\oplus$. We also find a drop of the efficiency of both the eccentricity and inclination driving for planetary masses larger than a few Earth masses, despite the large luminosity-to-mass ratio implied for these masses by our constant mass doubling time. For our mass doubling time of $\tau = 10^5$ kyrs, a planet will experience an eccentricity growth above the value $e_0 = 0.01$ up to a mass $M_{\max} \approx 5.7 M_\oplus$, and an inclination growth up to a mass marginally larger than our upper mass limit of $7.6 M_\oplus$ (extrapolating the data of Fig. 8 we obtain $M'_{\max} = 8.1 M_\oplus$).

Note that on the low-mass end of these graphs, the planet is essentially non-luminous, and we recover the vigorous damping of the eccentricity and inclination that we found in section 3.2, with dimensionless coefficients larger, in absolute value, than the analytic estimates of Tanaka & Ward (2004).

4.5 Temperature perturbations in the disc

We show in Fig. 9 the temperature difference between a run with a luminous planet and a run with a non-luminous planet, at the disc’s midplane, when the planet is at four different locations of its orbital motion. The parameters used here are those of the fiducial eccentric calculation. In this section only, the planet is not freely moving in the disc. Rather, it is held on a fixed eccentric orbit. Indeed, a luminous and non-luminous planet do not follow exactly the same trajectory, and subtracting the temperature fields of two runs where the planet is not exactly at the same location would be meaningless.

Fig. 10 shows similar plots for the case of the fiducial calculation of an inclined planet. In both cases, we see a “hot plume” trailing the planet. Note that the unperturbed disc’s midplane temperature at the planet’s location is $T_0 = 82$ K,

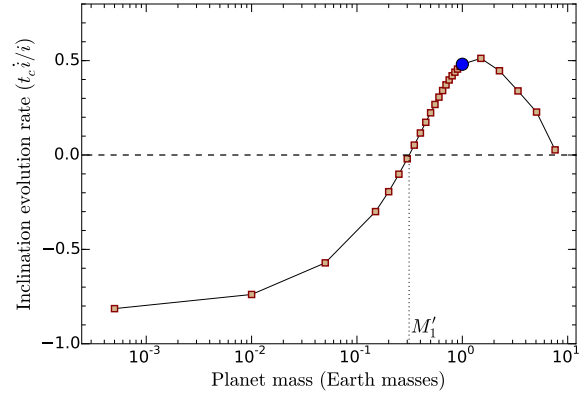


Figure 8. The evolution rate of inclination as a function of the planet mass. The mass doubling time has the fiducial value of $\tau = 10^5$ yrs.

so the relative temperature perturbation in the plume is at the $O(10^{-1})$ level. In order to compare the size of this plume to the expression given by Masset & Velasco Romero (2017), we require an estimate of the disc’s thermal diffusivity. We use the estimate given by Bitsch et al. (2014, their Eq. 16):

$$\chi = \frac{16\gamma(\gamma-1)\sigma T^4}{3\kappa(\rho_0 H \Omega_p)^2} \approx 4.6 \cdot 10^{15} \text{ cm}^2 \text{ s}^{-1} \text{ at } 5.2 \text{ au} \quad (8)$$

where ρ_0 is the disc’s midplane density. According to Masset & Velasco Romero (2017), the plume’s size depends on the planet’s velocity with respect to the ambient gas. At apor pericentre, this velocity is $a\Omega_p e/2$. Inserting this value in Eq. (24) of Masset & Velasco Romero (2017), we get for the plume’s cut-off length scale:

$$\lambda = \frac{2\chi}{\gamma a \Omega_p e} \sim 6.5 \cdot 10^{-3} a \sim 0.03 \text{ au}. \quad (9)$$

This length only occupies one zone in azimuth, four zones in radius and three zones in colatitude. The plume is therefore barely resolved, which suggests that the heating force it exerts on the planet is underestimated (according to Fig. 1 of Masset & Velasco Romero (2017), roughly half of the force comes from a distance larger than 2λ from the planet, and $\sim 80\%$ from a distance larger than λ). This cut off scale is much smaller than the disc’s pressure length scale H , and also smaller than the planet’s epicyclic excursion ae . This is in agreement with the visual examination of Figs. 9 and 10.

The heat released in the planet vicinity takes some time to diffuse within the plume. This time has been called the response time by Masset & Velasco Romero (2017), and has the expression:

$$\tau_{\text{diff}} \sim \frac{\lambda^2}{\chi} \sim \frac{\chi}{\gamma^2 V^2}, \quad (10)$$

where V is the perturber’s velocity with respect to the ambient gas. As the heat diffuses within the plume, the latter is simultaneously sheared by the Keplerian flow, over a time scale $(2A)^{-1} = (2/3)\Omega_p^{-1}$, where A is Oort’s first constant. The shear is unimportant if the response time is much smaller than the shear time scale. In these conditions, the force exerted by the heated region over the perturber is essentially

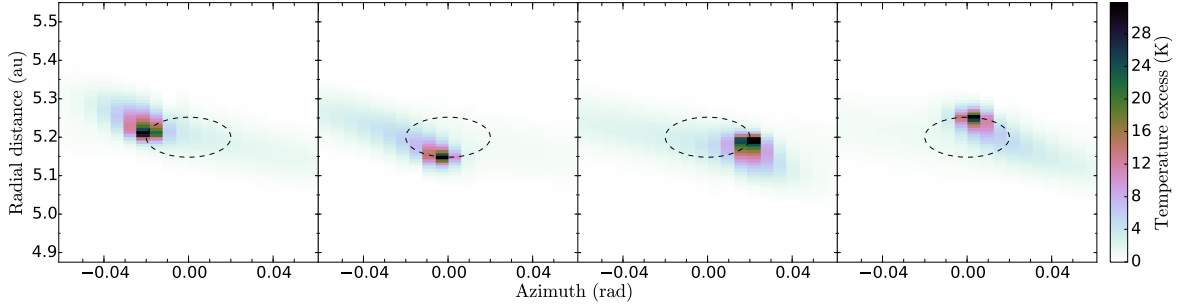


Figure 9. Temperature excess due to the heat release at the disc’s midplane, for an eccentric planet. The dotted ellipse represents the planet’s epicycle. The orbit’s guiding centre is at the centre of each plot. The second and fourth plots show the planet at the pericentre and apocentre, respectively. The time difference between successive plots is one fourth of the planet’s orbital period. A video of this sequence is available at the online version of this article.

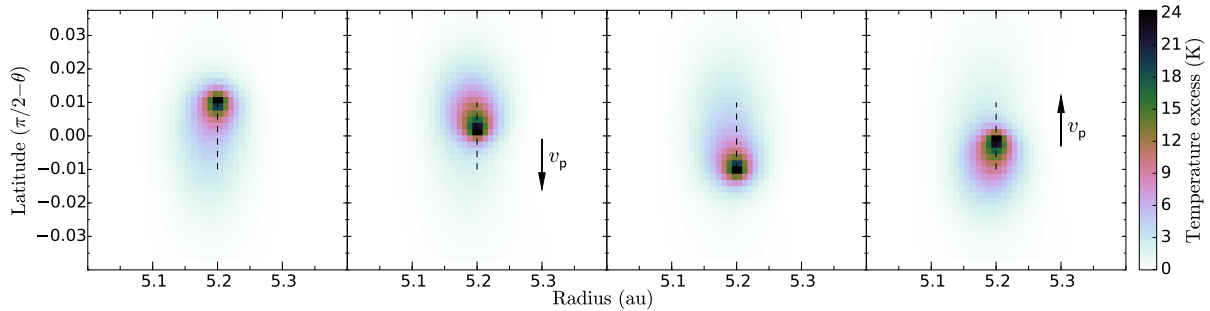


Figure 10. Temperature excess due to the heat release in the meridional (r, θ) plane, for an inclined planet. The dotted line represents the planet’s trajectory in this plane. The time difference between successive plots is one fourth of the planet’s orbital period. The arrows show the direction of the planetary motion. In the first and third plot, the planet has a vanishing vertical velocity. A video of this sequence is available at the online version of this article.

that given by a dynamical friction calculation. We refer to this regime as a headwind-dominated regime. The condition $\tau_{\text{diff}} \ll (2/3)\Omega_p^{-1}$ translates into $e \gg e_l$, with:

$$e_l = \frac{1}{\gamma} \left(\frac{6\chi}{a^2\Omega_p} \right)^{1/2} \approx 0.012, \quad (11)$$

where as above we have used $V = ae\Omega_p/2$. For eccentricities below this limit, the shape of the heated region is strongly affected by the shear. We refer to this regime as the shear-dominated regime. We comment that the limit eccentricity e_l can also be worked out by requiring that the cut-off length λ be equal to the distance between the planet and corotation at peri- or apocentre.

In the headwind-dominated regime the plume can essentially be regarded as a hot trail behind the planet as in Figs. 9 and 10. In the shear-dominated regime, it has a more complex shape with two lobes sheared apart by the flow: the heat that has diffused to smaller radii is advected toward positive azimuth, while the heat that has diffused to larger radii is advected toward negative azimuth. This is illustrated in Fig. 11. In the limit case of a circular orbit, one gets two lobes in steady state as found by Benítez-Llambay et al. (2015). In this case the most pronounced lobe resides on the same side of corotation as the planet.

4.6 Long-term behaviour

We focus now on the long-term evolution of embedded, hot planets. Given the large computational cost of each simulation presented in this section (they represent typically 1-2 months-GPU on our cluster), we present a limited number of such simulations. Note that although the total amount of time spanned by a given run may amount to a substantial fraction of the mass doubling time, we keep the planetary mass constant during our simulations. This inconsistency allows us to separate the behaviour arising from heating from the behaviour that would arise from an intrinsic mass growth.

4.6.1 Fiducial parameters

The study presented in section 4.2 suggests that the eccentricity and inclination would converge respectively toward e_c and i_c at larger time, for our fiducial parameters. We check whether this assumption is correct. Fig. 12 shows the long-term behaviour of the eccentricity, which is found to converge indeed toward e_c , regardless of its initial value. Although it does so in a globally smooth manner, the eccentricity is not strictly monotonous in time and exhibits low amplitude, non-periodic oscillations over time.

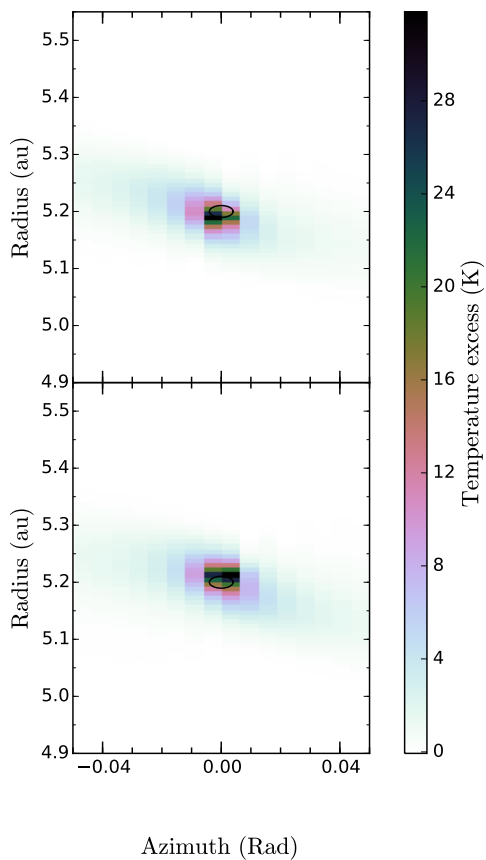


Figure 11. Temperature excess due to the heat release at the disc’s midplane, for a low eccentricity planet. The ellipse represents the planet’s epicycle. This figure has been obtained in the same manner as fig. 9, except that the planetary eccentricity is here $e = 2 \cdot 10^{-3}$. The planet is at pericentre in the top plot, and at apocentre in the bottom plot. A video of this case is available at the online version of this article.

Fig. 13 displays the behaviour of the inclination for the same disc and planet parameters. Initially, a trend similar to that of the eccentricity is found, in which the inclination tends toward the value of i_c found in section 4.2. However, the run with a low initial value of the inclination shows a reversal of the inclination trend at $t \approx 1500$ orbits. This behaviour occurs when the planet’s eccentricity becomes sizeable. The initial eccentricity of the planet indeed quickly levels off to a very small, non-vanishing value given by the perturbations induced in the disc by the planet, of the order of 10^{-6} . Subsequently, as can be seen in the inset plot of Fig. 13, the eccentricity grows exponentially. The growth rate of the eccentricity is found to depend on the inclination for this set of values (a simple explanation for this could be that the inclination is here comparable to the disc’s aspect ratio, hence the more inclined planet spends more time in rarefied regions of the disc where the interaction with the latter is weaker). The above results suggest that the driv-

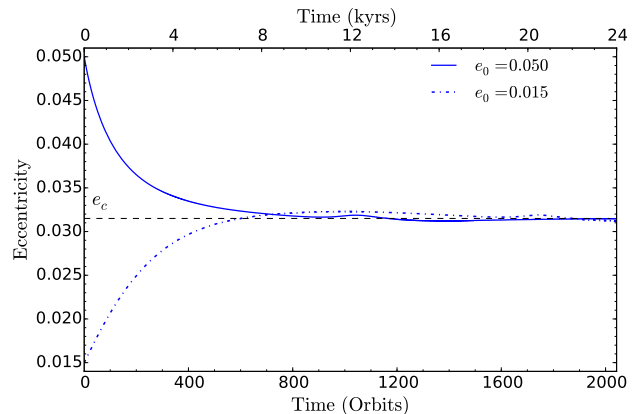


Figure 12. Evolution over 2000 orbits of the eccentricity for two different initial values, $e_0 = 0.015$ and $e_0 = 0.050$. In both cases the eccentricity converges towards e_c .

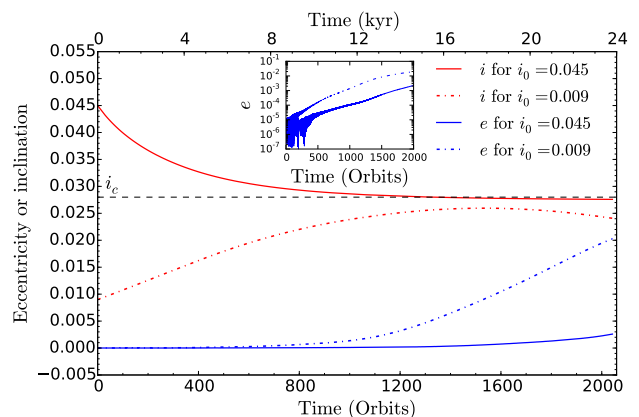


Figure 13. Evolution of the inclination over 2000 orbits, for two different initial values: $i_0 = 0.009$ and $i_0 = 0.045$. The blue lines (initially close to the x-axis) show the eccentricities in the corresponding runs, with a matching line style. The inset plot shows the eccentricity behaviour on a logarithmic scale.

ings of the inclination and eccentricity by the heating are somehow coupled.

4.6.2 Further results for a larger luminosity

We further explore this possibility by comparing the outcome of simultaneous eccentricity and inclination growth episodes with different starting values. In order to speed up the time evolution of the system in our different configurations, we adopt from now on a mass doubling time of 50 kyrs, a factor of two shorter than the fiducial value. All other parameters are those of the fiducial calculations. A consequence of the planet’s larger luminosity is that the asymptotic values of eccentricity and inclination are larger than the fiducial ones. We show in Fig. 14 the time evolution of the eccentricity and inclination for two different starting conditions: one in which $e_0 = i_0 = 10^{-5}$, and another one in which these values were set to zero, but quickly level off

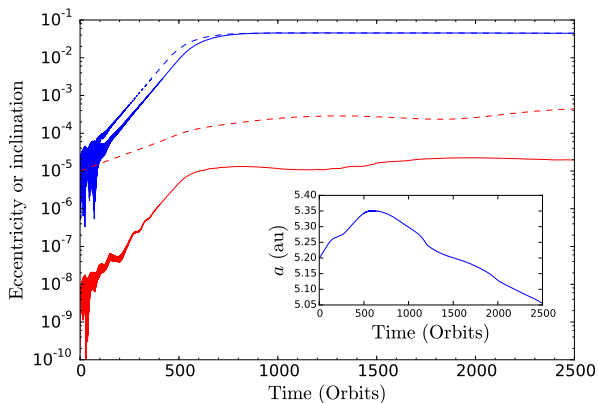


Figure 14. Long-term evolution of the eccentricity and inclination for an Earth mass planet with a doubling time $\tau = 50$ kyrs in our fiducial disc, for two different starting conditions: $(e_0, i_0) = (10^{-5}, 10^{-5})$ (dotted lines) and $(e_0, i_0) \sim (10^{-6}, 10^{-9})$ (solid lines). The two curves in the upper part of the diagram show the eccentricity (in blue in the electronic version), while the other two curves (in red in the electronic version) show the inclination with a matching line style. The inset plot shows the time behaviour of the semi-major axis of the planet of the second case.

to very small values because of the perturbation induced by the planet for the eccentricity (around $\sim 10^{-6}$) or because of numerical noise for the inclination (around 10^{-9}). In both cases the eccentricity displays a phase of exponential growth over several decades in the shear-dominated regime (which we had anticipated from the examination of Fig. 3), and then levels off toward an asymptotic value of 0.044. The inclination, on the contrary, exhibits a very different behaviour: after a phase of exponential growth (with a different growth rate in each case), it levels off at very low values, orders of magnitude smaller than its asymptotic value which can be inferred from an analysis similar to that of section 4.2, and which is ~ 0.04 . It is noteworthy that the inclination levels off when the eccentricity reaches sizeable values (≥ 0.01). This suggests that a value of the eccentricity close to the nominal value quenches the inclination growth.

Fig. 14 also shows the time behaviour of the semi-major axis of the planet which has initially $(e_0, i_0) \sim (10^{-6}, 10^{-9})$. In agreement with the results of Benítez-Llambay et al. (2015), the planet initially migrates outwards, and reverses its migration once its eccentricity has reached a sizeable value of ~ 0.01 . Although we have not investigated the reasons for this behaviour, it appears compatible with a substantial fraction of the total torque arising from a positive corotation torque, which is quenched once the radial excursion ae is larger than the half-width of the horseshoe region $x_s \approx 8 \cdot 10^{-3}a$ (Hellary & Nelson 2012). We comment that this migration behaviour may be affected by the bias mentioned in section 3.2.1, and that the total variation of the semi-major axis over the whole extent of this long-term run is minute, as anticipated.

We conclude this section by showing results in Fig. 15 for similar calculations, this time with $(e_0, i_0) = (10^{-6}, 0.01)$ and with $(e_0, i_0) = (0.01, 0.01)$. The former shows a behaviour similar to the one seen in Fig. 13, with an initial growth

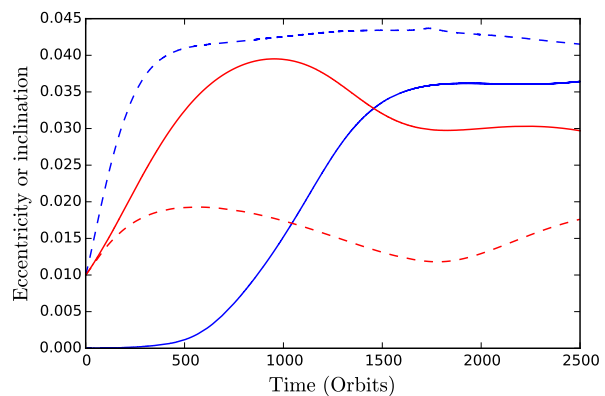


Figure 15. Results for calculations similar to those of Fig. 14 for $(e_0, i_0) = (0.01, 0.01)$ (dashed lines) and $(e_0, i_0) = (\sim 10^{-6}, 0.01)$ (solid lines). The eccentricity (inclination) curves appear in blue (red) on the electronic version.

of the inclination followed by a mild decay once the eccentricity has reached a sizeable value. At larger time the eccentricity and inclination appear to have plateaued toward nearly constant values, both smaller than their asymptotic values taken separately, the eccentricity being marginally larger than the inclination. The other calculation presented in this figure, which starts with $e_0 = i_0 = 0.01$, shows that the eccentricity grows toward a nearly constant value between 0.04 and 0.045, whereas the inclination has an initial growth rate smaller than in the other calculation, and never exceed 0.02. This clearly illustrates the interdependence of the time evolution of the eccentricity and inclination.

4.7 A toy model

We present here a toy model which reproduces some of the characteristics of the eccentricity and inclination growth in the headwind dominated regime. Under these conditions, the force on the planet arising from the heat release can be obtained by a dynamical friction calculation (Masset & Velasco Romero 2017).

The Hamiltonian of the planet in a frame corotating with its guiding centre is given, in spherical coordinates, by:

$$H = \frac{1}{2}M_p \dot{r}^2 + \frac{1}{2}M_p r^2 \sin^2 \theta \dot{\phi}^2 + \frac{1}{2}M_p r^2 \dot{\theta}^2 - \frac{1}{2}M_p r^2 \sin^2 \theta \Omega_p^2 - \frac{GM_\star M_p}{r}, \quad (12)$$

where ϕ is the azimuthal angle between the guiding centre and the planet. We assume from now on that the angular velocity of the guiding centre is fixed, or equivalently that the planet does not migrate. The migration timescale is typically two to three orders of magnitude larger than the eccentricity and inclination evolution timescales (Artymowicz 1993; Tanaka et al. 2002; Tanaka & Ward 2004), even when the planet releases heat (Benítez-Llambay et al. 2015), so this assumption is reasonable. When the planet is subjected to a non-conservative force (F_r, F_ϕ, F_θ) , its Hamiltonian varies in time at the rate:

$$\dot{H} = \dot{r}F_r + r \sin \theta \dot{\phi}F_\phi + r \dot{\theta}F_\theta, \quad (13)$$

where the right hand side represents the work of the force in the frame corotating with the guiding centre. The planetary orbit, to first order in e and i , reads:

$$\begin{cases} r = a[1 + e \cos(\Omega_p t + \varphi)] \\ \phi = 2e \sin(\Omega_p t + \varphi) \\ \theta = \frac{\pi}{2} - i \sin(\Omega_p t), \end{cases} \quad (14)$$

where φ is an arbitrary phase and where we have adopted, without loss of generality, $t = 0$ on the ascending line of nodes. Upon substitution of these expressions in Eq. (12), we obtain:

$$H = H_c + \frac{1}{2} a^2 \Omega_p^2 (e^2 + i^2), \quad (15)$$

where $H_c = -(3/2)a^2\Omega_p^2$ is the value of H when the planet is on a circular, non-inclined orbit. The impact of the heating force on the orbital elements can be evaluated by averaging its work in the rotating frame over one orbital period. [Masset & Velasco Romero \(2017\)](#) have shown that in the low Mach number limit the force does not depend on the perturber's velocity. Here we assume the force to be a constant F_0 , and to be directed along the velocity vector of the planet relative to the ambient gas. When the planet is inclined and non-eccentric, the work is obtained readily as:

$$W_i = 4F_0 a i. \quad (16)$$

Equating this work to the variation of H over one orbital period, we can write the time derivative of the inclination:

$$\frac{di}{dt} = \frac{2F_0}{\pi a M_p \Omega_p} \approx 0.64 \frac{F_0}{a M_p \Omega_p} \quad (17)$$

We now consider an eccentric, non-inclined planet. Using the notation: $x = r - a$ and $y = a\phi$, we can write to lowest order in e , with an arbitrary choice of the time origin:

$$\mathbf{q} = (x, y) = [ae \sin(\Omega_p t), 2ae \cos(\Omega_p t)] \quad (18)$$

The gas velocity is $[0, (-3/2)\Omega_p x]$, hence the planet's velocity in the gas frame reads:

$$\mathbf{v}' = (v'_x, v'_y) = ae\Omega_p [\cos(\Omega_p t), -(1/2)\sin(\Omega_p t)]. \quad (19)$$

The work of the heating force over the epicycle is therefore:

$$\begin{aligned} W_e &= \oint F_0 \frac{\mathbf{v}' \cdot d\mathbf{q}}{v'} = \int_0^{2\pi} \frac{F_0 ae \Omega_p dt}{[\cos^2(\Omega_p t) + \sin^2(\Omega_p t)/4]} \\ &= 8.63 F_0 ae. \end{aligned} \quad (20)$$

From this work we can deduce the time derivative of the eccentricity:

$$\frac{de}{dt} \approx 1.37 \frac{F_0}{a M_p \Omega_p}. \quad (21)$$

Eqs. (17) and (21) show that in the headwind-dominated regime, the eccentricity and inclination should experience a linear growth. This is compatible with the graphs of Fig. 15.

We could extend this study by adding to the work of the non-conservative force the contribution of the disc's tide, so as to match the damping rates given by [Tanaka & Ward \(2004\)](#) or those, more recent, of [Cresswell et al. \(2007\)](#). Our preliminary study of section 3.2 shows nevertheless that the damping rates in a radiative disc are at odds with those given for isothermal discs. On general grounds, however, we

note that the exponential or nearly exponential damping of e (i) by the disc's tide implies that the work of the tide should be negative and scale as e^2 (i^2), i.e. faster than that of the heating force. For values of e (i) lower than e_c (i_c), the work of the heating force dominates and the orbital element grows, until reaching the value (e_c or i_c) at which the tide's work cancels out the work of the heating force. At this point the orbital element remains constant in time.

The work of Eq. (20) is only 11 % smaller than the estimate that would be obtained assuming that the force is tangent everywhere to the epicycle. This remark allows to understand why the impact of the force is larger on eccentricity than on inclination: it is simply because the epicycle circumference is significantly larger than (twice⁴) the length of the arc described by an inclined planet, for configurations where the eccentricity and inclination have same values. This results in the heating force exerting more work on an eccentric planet, over one orbital period.

In this toy model the ratio of the eccentricity to inclination time derivative is 2.2, smaller than the ratio of ~ 3 that we found in our simulations. Many factors can account for this difference:

- Our toy model calculation assumes that the response time of the heating force is vanishingly small.
- It also assumes the heating force to be independent of altitude, whereas the sound speed and thermal diffusivity (variables that come into play in the expression of the heating force) depend on altitude.
- We have a low, anisotropic resolution, so the heating force in our numerical simulations can have a different value for different directions of motion.
- Our toy model neglects the damping effect of the disc tide on the eccentricity and inclination.

Nevertheless, our calculation suggests that the stronger impact on eccentricity should be a rather general outcome, and not a particular result arising from the specifics of our fiducial disc model.

If we now consider a planet that is both eccentric and inclined, it is still subjected to a heating force of magnitude F_0 , the horizontal projection of which drives the eccentricity, while its vertical projection drives the inclination. The effect on both orbital elements is therefore necessarily weaker than the effect obtained when considering each orbital element in isolation, *i.e.* when the planet is either only eccentric or only inclined. Furthermore, the ratio of the vertical to horizontal component of the heating force is $\sim i/e$. If the planet has an eccentricity much larger than its inclination, it is left with a very small vertical component of the force to drive the inclination, which is counteracted at low values by the disc's tide. This simple model therefore broadly accounts for the salient features of the long-term behaviours that have been presented in sections 4.6.1 and 4.6.2. It also suggests that the asymptotic value of the orbital elements should depend on L/M_p if they result from a balance between the heating force (which scales as LM_p) and the disc's tide (which scales as M_p^2).

⁴ Over one orbital period the motion is alternatively downward and upward.

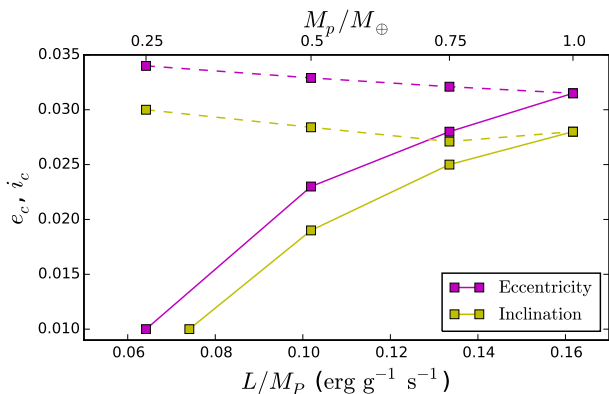


Figure 16. Asymptotic values of the eccentricity (magenta in the electronic version) and inclination (yellow in the electronic version) as a function of the planetary mass for a constant mass doubling time (solid lines) and for a constant luminosity to mass ratio (dashed lines). The bottom axis only refers to the solid lines, since the data of the dashed lines has been obtained for a constant value of $L/M_p = 0.16 \text{ erg g}^{-1} \text{ s}^{-1}$.

4.7.1 Planetary mass

In order to check this hypothesis, we study here the asymptotic value of the eccentricity and inclination as a function of the planetary mass, for our fiducial parameters. This value is determined by a dichotomic search of the value of e or i that leads to a negligible variation of the orbital element over 5 orbits. We have seen in section 4.6 that this is not necessarily the value toward which the orbital element will converge, especially for the inclination, which, in a calculation with small initial values of the orbital elements, is overrun by the eccentricity and levels off at low values. It provides nonetheless an estimate of the maximum value that one can expect for the orbital elements.

We show two kinds of dependencies in Fig. 16. One is obtained by varying the planetary mass with a constant mass doubling time. The other one is obtained by varying the planetary mass and the mass doubling time so as to have a constant luminosity to mass ratio, equal to that of the fiducial run ($L/M_p = 0.16 \text{ erg g}^{-1} \text{ s}^{-1}$). This second series shows nearly constant orbital parameters, which implies that, for given disc parameters, their asymptotic value essentially depends on the luminosity to mass ratio, as suggested in section 4.7. On the contrary, in the first series, the dependence of the orbital parameters on the planetary mass reflects the variation of the luminosity to mass ratio of the planet. We comment that our fiducial luminosity to mass ratio is nearly two orders of magnitude larger than the specific heating rate due to the decay of ^{26}Al at the CAI formation (e.g. Ghosh et al. 2006, and refs. therein). Therefore, an embryo solely heated by ^{26}Al decay would not be luminous enough to experience a growth of eccentricity or inclination.

5 DISCUSSION

As we have mentioned in section 4.5, the resolution employed in this study is barely sufficient to describe the planetary

hot trail. Fig. 1 of Masset & Velasco Romero (2017) shows that an accurate estimate of the heating force requires to resolve scales that are much smaller than the cut-off length λ , which is not the case here. Using Eqs. (17) and (21) with the estimate of the heating force given at low Mach number by Masset & Velasco Romero (2017) leads to growth rates several times in excess of those found in section 4.1, which suggests that the heating force is indeed largely underestimated in our present setup.

On the other hand, a more refined treatment of the planetary accretion may imply a reduced planetary luminosity and ultimately lower eccentricity and inclination growth rates. Our simple expression of the luminosity (Eq. 2) assumes that all the potential energy of the accreted material is radiated instantaneously, and translates into an effective temperature:

$$T_{\text{eff}} = 1220 \left(\frac{M_p}{M_\oplus} \right)^{1/4} \left(\frac{\rho_p}{3 \text{ g cm}^{-3}} \right)^{1/4} \left(\frac{\tau}{100 \text{ kyrs}} \right)^{-1/4} \text{ K.} \quad (22)$$

In a different context, that of the atmosphere of Earth-like planets after giant impacts, Lupu et al. (2014) show that the effective temperature of the planet may be substantially smaller than its surface temperature due to the blanketing by the atmosphere, delaying the planet’s cooling. Should an accreting embryo be subjected to a similar blanketing, the efficiency of our driving mechanism would be lowered. For a given maximal effective temperature, smaller embryos would have a larger luminosity to mass ratio, since the luminosity scales as R_p^2 and the mass as R_p^3 .

The Bondi sphere of our fiducial $1 M_\oplus$ planet is unresolved. The flow is non-linear and has a complex structure at the sub-Bondi scale (Fung et al. 2016, 2015). The force arising from the hot gas within the Bondi sphere is not captured by our analysis and is presently unknown. This underlines the need for very high resolution calculations in the planet vicinity, which would probably need either nested meshes (Szulágyi et al. 2016) or freely moving meshes (Muñoz et al. 2014) to meet the demanding resolution requirements. We note that if the diffusion timescale of the heat across the Bondi radius is smaller than the acoustic time across the Bondi radius, the dynamical impact of the heat release within the Bondi radius should be limited. This occurs when $M_p < 4\chi c_s/G = 2.5 M_\oplus$ for our fiducial disc.

We find a cut-off of the excitation of eccentricity and inclination past values of $\geq 1 M_\oplus$. This cut-off is similar to that found by Benítez-Llambay et al. (2015) for migration. From considerations on the yield of the conversion of the planet’s luminosity into kinetic energy, Masset & Velasco Romero (2017) argue that the magnitude of the heating force must decay when $GM/\chi c_s \gtrsim 1$. This threshold is in broad agreement with the numerical value quoted above. A deeper understanding of this cut-off definitely requires a resolved calculation of the flow at the sub-Bondi scale.

Masset & Velasco Romero (2017) have speculated that planets with a large luminosity to mass ratio could undergo indefinite eccentricity driving, resulting in the planet being supersonic with respect to the gas. We have not found such outcome for any reasonable value of the planetary luminosity in our setup. However, the plume size decreases when the velocity of the planet relative to the gas increases. Our lack of supersonic planets may therefore simply reflect our lack

of resolution, and stresses again the need for calculations at very high resolution.

6 CONCLUSIONS

We find that Earth-sized planetary embryos heated by accretion and embedded in opaque protoplanetary discs can experience eccentricity and inclination growth to values that are comparable to the disc's aspect ratio, over timescales of the order of a few kyrs, for luminosities corresponding to mass doubling times of order of 10^5 yrs. The asymptotic value depends on the luminosity to mass ratio of the planet. However, a more refined treatment of the planetary luminosity, and higher resolution calculations are required to accurately determine the ultimate values of the eccentricity and inclination.

The origin of this growth is the appearance of a hot, underdense region in the planet vicinity. The size of this region, for the parameters that we considered, is significantly smaller than the disc's pressure scale length. As a consequence, the transition between a shear-dominated regime (in which this region is sheared apart by the Keplerian flow) to a headwind-dominated regime (for which the Keplerian shear becomes unimportant) occurs for values of the eccentricity significantly smaller than the disc's aspect ratio (at $e \sim 0.01$ for our set of parameters). In the headwind-dominated regime, we expect a heating force similar to that described by [Masset & Velasco Romero \(2017\)](#) to act on the planet. The value reached at larger time by the eccentricity or inclination is set by the balance between the heating force, which excites the orbital element, and the disc's tide, which damps it.

We find that the drivings of the eccentricity and inclination by heating are coupled at larger time. Our interpretation is as follows. In the headwind-dominated regime, the heating force is nearly constant. Its horizontal projection drives the eccentricity, while its vertical projection drives the inclination. The values reached at larger time by these orbital elements, when the planet is both eccentric and inclined, are therefore smaller than the values reached by a planet that is either only eccentric, or only inclined, since only a fraction of the (constant) heating force contributes to the driving of each of these orbital element. This accounts for the coupling of the eccentricity and inclination evolutions.

We find that the eccentricity has a growth rate approximately three times larger than that of the inclination. When a planet has initially a very small eccentricity and inclination, the eccentricity overruns the inclination, and the planet reaches the headwind-dominated regime with a very low value of the inclination. It is then subjected to a nearly horizontal heating force, which quenches any further growth of the inclination. The outcome is therefore a planet with a significant eccentricity (comparable to the disc's aspect ratio) and a very small inclination. When, on the contrary, the planet has initially a sizeable inclination, it will remain sizeable, and at larger time the eccentricity and inclination will have same order of magnitude.

Extensions of this work could be an assessment of the actual luminosity of embryos, and the derivation of analytical prescriptions for the effect of heat release on eccentricity and inclination, so as to evaluate its impact on scenarios of

dynamical relaxation and collisions of a set of protoplanetary embryos.

As a side result, we find damping rates of eccentricity and inclination on a non-luminous planet, in a radiative disc, that are significantly larger than those found in isothermal discs.

ACKNOWLEDGEMENTS

H. Eklund wishes to thank the Linnaeus-Palme exchange program for their support, and the *Instituto de Ciencias Físicas* of UNAM for support and hospitality. The authors acknowledge CONACyT grant 178377 and UNAM's PAPIIT grant 101616. The authors thank the referee for a constructive report and J. Szulágyi for a thorough reading of a first draft of this manuscript.

REFERENCES

- Artymowicz P., 1993, *ApJ*, **419**, 166
 Baruteau C., Masset F., 2008, *ApJ*, **678**, 483
 Benítez-Llambay P., Masset F. S., 2016, *ApJS*, **223**, 11
 Benítez-Llambay P., Masset F., Koenigsberger G., Szulágyi J., 2015, *Nature*, **520**, 63
 Bitsch B., Kley W., 2010, *A&A*, **523**, A30
 Bitsch B., Kley W., 2011, *A&A*, **530**, A41
 Bitsch B., Crida A., Morbidelli A., Kley W., Dobbs-Dixon I., 2013, *A&A*, **549**, A124
 Bitsch B., Morbidelli A., Lega E., Crida A., 2014, *A&A*, **564**, A135
 Cresswell P., Dirksen G., Kley W., Nelson R. P., 2007, *A&A*, **473**, 329
 Fung J., Artymowicz P., Wu Y., 2015, *ApJ*, **811**, 101
 Fung J., Masset F., Lega E., Velasco D., 2016, preprint, ([arXiv:1610.09375](#))
 Ghosh A., Weidenschilling S. J., McSween Jr. H. Y., Rubin A., 2006, *Asteroidal Heating and Thermal Stratification of the Asteroidal Belt*. University of Arizona Press, pp 555–566
 Hellary P., Nelson R. P., 2012, *MNRAS*, **419**, 2737
 Lambrechts M., Johansen A., 2012, *A&A*, **544**, A32
 Lupu R. E., et al., 2014, *ApJ*, **784**, 27
 Masset F., 2000, *A&AS*, **141**, 165
 Masset F. S., 2001, *ApJ*, **558**, 453
 Masset F. S., Casoli J., 2010, *ApJ*, **723**, 1393
 Masset F. S., Velasco Romero D. A., 2017, *MNRAS*, **465**, 3175
 Muñoz D. J., Kratter K., Springel V., Hernquist L., 2014, *MNRAS*, **445**, 3475
 Muto T., Takeuchi T., Ida S., 2011, *ApJ*, **737**, 37
 Paardekooper S.-J., Papaloizou J. C. B., 2009, *MNRAS*, **394**, 2283
 Paardekooper S., Baruteau C., Kley W., 2011, *MNRAS*, **410**, 293
 Papaloizou J. C. B., 2002a, *A&A*, **388**, 615
 Papaloizou J. C. B., 2002b, *A&A*, **388**, 615
 Papaloizou J. C. B., Larwood J. D., 2000, *MNRAS*, **315**, 823
 Pollack J. B., Hubickyj O., Bodenheimer P., Lissauer J. J., Podolak M., Greenzweig Y., 1996, *Icarus*, **124**, 62
 Shakura N. I., Sunyaev R. A., 1973, *A&A*, **24**, 337
 Szulágyi J., Masset F., Lega E., Crida A., Morbidelli A., Guillot T., 2016, *MNRAS*, **460**, 2853
 Tanaka H., Ward W. R., 2004, *ApJ*, **602**, 388
 Tanaka H., Takeuchi T., Ward W. R., 2002, *ApJ*, **565**, 1257

This paper has been typeset from a $\text{\TeX}/\text{\LaTeX}$ file prepared by the author.